Ocean Systems Engineering, *Vol. 14, No. 4 (2024) 405-420*
https://doi.org/10.12989/ose.2024.14.4.405

Global behavior monitoring of underwater lines using generalized coordinate based polynomial equations and sensor fusion

Chungkuk Jin[1], Ikjae Lee[2], Moo Hyun Kim[*2] and Seong Hyeon Hong[3]

[1]Department of Ocean Engineering and Marine Sciences, Florida Institute of Technology, 150 W University Blvd, Melbourne, FL 32901, USA
[2]Department of Ocean Engineering, Texas A&M University, Haynes Engineering Building, 727 Ross St, College Station, TX 77843, USA
[3]Department of Mechanical and Civil Engineering, Florida Institute of Technology, 150 W University Blvd, Melbourne, FL 32901, USA

(Received September 23, 2024, Revised December 12, 2024, Accepted December 15, 2024)

Abstract. A line-monitoring methodology employing cubic polynomial equations and sensor fusion has been developed to evaluate the global behavior and stress distribution of underwater lines. The approach integrates generalized coordinates with a single global coordinate framework to efficiently and conveniently capture the behavior of geometrically complex lines. The system requires input data including displacements and curvatures at both ends and inclinations along the line, which serve as boundary conditions for the polynomial equations. Using the computed global displacements, other stress-related variables, such as tensile, bending, and nominal stresses, can subsequently be estimated. To validate the proposed methodology, two numerical case studies—a submerged inclined tunnel and a lazy-wave riser—were conducted. Results indicate that the global behavior of the underwater lines is accurately recovered when a sufficient number of sensors are employed although its accuracy can be diminished with less number of sensors. Stress estimation demonstrated higher precision in the submerged inclined tunnel compared to the lazy-wave riser due to the latter's pronounced initial curvature and sharp transitions near the touchdown zones.

Keywords: global behavior; global stress; inclinometers; polynomial equations; riser monitoring; sensor fusion

1. Introduction

Slender underwater structures such as production risers, drilling risers, subsea pipelines, underwater cables, and underwater tunnels are essential for offshore operations and the transportation of resources and personnel. Despite their importance, monitoring the structural integrity of these components poses significant challenges. Issues such as ensuring a consistent power supply, establishing reliable data communication, and conducting visual inspections using expensive equipment like remotely operated vehicles (ROVs) and underwater robots complicate the

*Corresponding author, Professor, E-mail: m-kim3@tamu.edu

http://www.techno-press.org/?journal=ose&subpage=7 ISSN: 2093-6702 (Print), 2093-677X (Online)

process. As a result, developing a robust methodology for global structural health monitoring that is both accurate and cost-effective is essential.

This study proposes a methodology for global stress monitoring of flexible, line-like underwater structures, with a focus on assessing their global behaviors, stress levels, and accumulated fatigue damage. Previous research has proposed a variety of approaches and sensor technologies for monitoring underwater line-like structures. In terms of methodology, the modal decomposition and reconstruction (MDR) technique leverages the principle of superposition to calculate global displacements and stresses along a structure by combining modal displacements and eigenvalues (or Fourier series) (Kaasen and Lie 2003, McNeill and Agarwal 2011, Mukundan *et al*. 2010, Saruhashi *et al*. 2013). Another method, referred to as the transfer function (TF) method, involves using TFs to convert acceleration power spectral density (PSD) into bending moment PSD, facilitating the evaluation of global stress and fatigue damage (Bakker 2011, Mercan *et al.* 2021, Wang *et al.* 2023). These TFs can be derived either analytically or using finite element simulations. Both the MDR and TF methods have been widely used for vertical risers, primarily relying on accelerometers, with angular rate sensors also being considered. Moreover, polynomial equations were proposed to estimate global behavior and stress, and coefficients in the polynomial equations were obtained by sensor data from inclinometers (Choi and Kim 2018, Chung *et al.* 2021), which can be applicable to both vertical and curved risers like catenary risers and lazy-wave risers. Compared with the MDR and TF methods, each time step has a unique set of polynomial coefficients, which is easier in real-time monitoring. Furthermore, advanced techniques such as finite-element-based digital twins and machine learning have recently emerged as promising solutions to minimize the number of required sensors (Chen *et al*. 2024, Chung *et al*. 2022, Jin *et al*. 2024, Kharazmi *et al*. 2021, Lee *et al*. 2024, Mao *et al.* 2022, Min *et al*. 2023).

This study advances the methodology for utilizing polynomial equations and inclinometer data in line-dynamics monitoring. Choi and Kim (2018) employed cubic polynomial equations to analyze vertical risers, estimating their in-plane behaviors using multiple inclinometers based on the assumption that the displacements at the top and bottom were known. To solve the cubic polynomial equations, a linear length equation was introduced as an additional equation. Similarly, Chung *et al.* (2021), proposed a global displacement framework for curved risers using quadratic polynomial equations with multiple bi-axial inclinometers, wherein displacements were sequentially calculated from the top. This method still necessitated a quadratic-line length equation as an extra condition. The use of this known initial length for each segment as an extra equation may introduce a nontrivial error when the dynamic elongation of the line is not small.

In the present study, generalized and single global coordinate systems, inspired by the rod theory framework introduced by Garrett (1982), were utilized to define the behavior of the line. This approach enables the efficient estimation of global behaviors and stresses for geometrically nonlinear lines without the need for coordinate transformations. Cubic polynomial equations were employed under the assumption of known displacements and curvatures at both ends, along with inclinations distributed along the line. Moreover, this research introduced comprehensive formulations for calculating the nominal stress from tensile and bending stresses within the generalized coordinate framework.

The paper is structured as follows: Section 2 details the proposed methodology for the line monitoring system, while Section 3 explains case studies—an underwater inclined tunnel and a lazy-wave riser. In Section 4, the results are analyzed, accompanied by a discussion of key findings. Specifically, the envelopes of root-mean-square error (RMSE), standard deviation (STD), and maxima (MAX), along with the time histories of global displacements and stresses, are presented

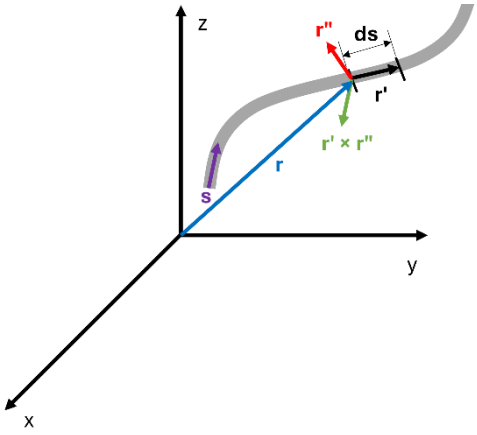

Fig. 1 Coordinate system

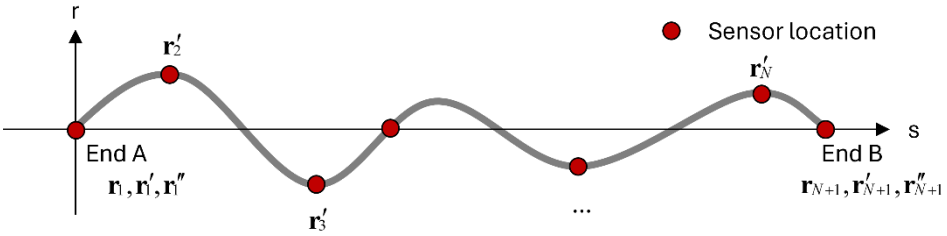

Fig. 2 Known boundary conditions from sensor measurements where N is the number of sensor positions

and discussed. Finally, Section 5 concludes the study and outlines potential directions for future research.

2. Method

The coordinate system is represented in Fig. 1. A generalized coordinate system was utilized to define displacements and stresses of a space curve in the *x*, *y*, and *z* directions. Vectors were defined in the single global coordinate system. In this coordinate system, a position vector $\mathbf{r}$ is a function of space and time; a unit tangent vector $\mathbf{r}'$ is a spatial derivative of the position vector where a prime denotes spatial derivative; a principal normal vector $\mathbf{r}''$ is a double spatial derivative of the position vector; and a bi-normal vector $\mathbf{r}' \times \mathbf{r}''$ is the cross product of the unit tangent vector and the principal normal vector, which means that the bi-normal vector is normal to both the unit tangent vector and the principal normal vector. The unit tangent and principal normal vectors are relevant to angle and curvature, respectively.

Known boundary conditions from sensor measurements are illustrated in Fig. 2. The developed monitoring system utilized boundary conditions from sensors to solve coefficients of cubic polynomial equations. For example, in the typical riser system, displacements at both ends can be known; time histories of displacements at the riser top section (END A) can be collected if we

measure platform motions; those of displacements at the bottom section (END B) are fixed for production. Curvatures at both ends can be measured by curvature sensors. Angles along the lines can be measured by inclinometers. The conversion from curvature and angles to unit tangent and principal normal vectors is straightforward and, therefore, not elaborated in this paper.

One finite element was placed between neighboring sensors, and a cubic polynomial equation was formulated to define displacements in the *x*, *y*, and *z* directions, separately. Then, based on the generalized coordinate system's properties, the following equations were established for the *i*-th finite element.

$$\mathbf{r}_i = \mathbf{a}_i s_i^3 + \mathbf{b}_i s_i^2 + \mathbf{c}_i s_i + \mathbf{d}_i \tag{1}$$

$$\mathbf{r}_i' = 3\mathbf{a}_i s_i^2 + 2\mathbf{b}_i s_i + \mathbf{c}_i \tag{2}$$

$$\mathbf{r}_i'' = 6\mathbf{a}_i s_i + 2\mathbf{b}_i \tag{3}$$

where s is the arc length of i-th finite element in the range of ($0 \le s_i \le L_i$) where L_i is the length of i-th finite element; **a**, **b**, **c**, and **d** are coefficients to define the space curve. Note that a cubic polynomial equation results in curvature defined as a linear equation. Some errors in curvature calculation may occur for complex curves like catenary and lazy-wave risers if sparse sensor intervals are adopted. Coefficients, **a**, **b**, **c**, and **d** are described in a vector form, which means that each *x*, *y*, or *z* displacement has a unique combination of these coefficients. To obtain these coefficients, global equations in the matrix and vector forms were established as

$$[\mathbf{K}]\{\mathbf{A}\} = \{\mathbf{f}\} \tag{4}$$

The matrix [**K**] includes values in front of coefficients defined by putting locations at both ends; and the vector $\{\mathbf{A}\}$ includes the coefficients to be solved, while the vector $\{\mathbf{f}\}$ contains all known boundary conditions. Again, each direction had one unique global equation; three global equations

Position vector ($s_1 = 0$)	$\rightarrow$	$\mathbf{d}_1 = \mathbf{r}_1$
Principal normal vector ($s_1 = 0$)	$\rightarrow$	$2\mathbf{b}_1 = \mathbf{r}_1''$

(a) First element (Element 1)

Position vector ($s_N = L_N$)	$\rightarrow$	$\mathbf{a}_N L_N^3 + \mathbf{b}_N L_N^2 + \mathbf{d}_N = \mathbf{r}_{N+1} - \mathbf{r}_N' L_N$
Unit tangent vector ($s_N = L_N$)	$\rightarrow$	$3\mathbf{a}_N L_N^2 + 2\mathbf{b}_N L_N = \mathbf{r}_{N+1}' - \mathbf{r}_N'$
Principal normal vector ($s_N = L_N$)	$\rightarrow$	$6\mathbf{a}_N L_N + 2\mathbf{b}_N = \mathbf{r}_{N+1}''$

(b) Last element (Element N)

Position vector ($s_i = L_i$)	$\rightarrow$	$\mathbf{a}_i L_i^3 + \mathbf{b}_i L_i^2 + \mathbf{d}_i - \mathbf{d}_{i+1} = -\mathbf{r}_i' L_i$
Unit tangent vector ($s_i = L_i$)	$\rightarrow$	$3\mathbf{a}_i L_i^2 + 2\mathbf{b}_i L_i = \mathbf{r}_{i+1}' - \mathbf{r}_i'$
Principal normal vector ($s_i = L_i$)	$\rightarrow$	$6\mathbf{a}_i L_i + 2\mathbf{b}_i - 2\mathbf{b}_{i+1} = 0$

(c) Continuity conditions (i = 1,2, …, N–1)

Fig. 3 Equations with known boundary conditions at the first and last finite elements (a) and (b) and for continuity conditions (c)

were required to obtain the position vectors in the *x*, *y*, and *z* directions. Fig. 3 explains how the global equation was obtained from known boundary and continuity conditions. The matrix construction followed a similar manner to cubic spline functions. Equations considered in the matrix were only included in Fig. 3. While cubic spline functions use displacements at both ends as boundary conditions, the present algorithm employed unit tangent vectors as boundary conditions. Continuity conditions for the position, unit tangent vectors, and principal normal vectors were also established at each shared node to ensure smooth transitions along the line. The basic idea of these continuity conditions is that position, unit tangent, and principal normal vectors of the last nodal location of *i*-th finite element are identical to those of the first nodal location of *i*+1-th finite element. This ensures a seamless connection between adjacent elements. Boundary conditions from inclinometers were taken into account at relevant nodes. In particular, since $\mathbf{c}_i$ can directly be obtained from the unit tangent vector at $s_i = 0$ such that $\mathbf{c}_i = \mathbf{r}_i'$, they were not solved in the matrix. In addition, supplementary boundary conditions from the known position and principal normal vectors were applied at both ends of the line.

From Fig. 3, Eq. (4) can be expressed as the following global matrix

$$\begin{Bmatrix}
 & & 1 & & & & & & & \\
 & 2 & & & & & & & & \\
L_1^3 & L_1^2 & 1 & & & -1 & & & & \\
3L_1^2 & 2L_1 & & & & & & & & \\
6L_1 & 2 & & & -2 & & & & & \\
 & & & L_2^3 & L_2^2 & 1 & & & & \\
 & & & 3L_2^2 & 2L_2 & & \cdots & & & \\
 & & & 6L_2 & 2 & & & & & \\
 & & & & \vdots & & \ddots & & & \\
 & & & & & & & L_N^3 & L_N^2 & 1 \\
 & & & & & & & 3L_N^2 & 2L_N & \\
 & & & & & & & 6L_N & 2 &
\end{Bmatrix}
\begin{Bmatrix}
\mathbf{a}_1 \\ \mathbf{b}_1 \\ \mathbf{d}_1 \\ \mathbf{a}_2 \\ \mathbf{b}_2 \\ \mathbf{d}_2 \\ \vdots \\ \mathbf{a}_N \\ \mathbf{b}_N \\ \mathbf{d}_N
\end{Bmatrix} =
\begin{Bmatrix}
\mathbf{r}_1 \\ \mathbf{r}_1'' \\ -\mathbf{r}_1' L_1 \\ \mathbf{r}_2' - \mathbf{r}_1' \\ 0 \\ -\mathbf{r}_2' L_2 \\ \mathbf{r}_3' - \mathbf{r}_2' \\ 0 \\ \vdots \\ \mathbf{r}_{N+1} - \mathbf{r}_N' L_N \\ \mathbf{r}_{N+1}' - \mathbf{r}_N' \\ \mathbf{r}_{N+1}''
\end{Bmatrix} \tag{5}$$

The vector $\{\mathbf{A}\}$ can mathematically be solved by the following equation using the pseudo inverse matrix

$$\{\mathbf{A}\} = [\mathbf{K}]^{+} \{\mathbf{f}\} \tag{6}$$

where + denotes the operator for the pseudo inverse. Due to the non-square nature of the matrix [**K**], the least squares method was employed to solve the system of equations, ensuring an optimal fit for the continuity and boundary constraints. Once $\{\mathbf{A}\}$ vectors in *x*, *y*, and *z* directions are obtained, displacements, unit tangent vectors, and principal normal vectors at any point of the line can be obtained by inputting corresponding coefficients into Eqs. (1)-(3).

Next, a critical aspect of line monitoring is the assessment of stress and fatigue damage. According to the DNV standard (DNV, 2010), the fatigue damage of the riser is calculated by using

the nominal stress that consists of contribution from tensile and bending stresses. While tensile stresses can in principle be obtained by line extension and internal and external pressure effects, a small extension can result in a significant difference in tension. In this regard, progressive calculations of tension were achieved by assuming that top tension can be measured by a device such as a load cell. Given the line tension at the k-th nodal position T_k, the following equations were employed to determine tension at the k+1 nodal position T_{k+1} and corresponding tensile stress σ_T (DNV 2010, Jin *et al.* 2015, Kim *et al*. 2021)

$$T_{k+1} = T_k + \mathbf{W} \cdot \mathbf{r}'_{k+0.5} + m_e \ddot{r}^t_{k+0.5}, \tag{7}$$

$$\sigma_T = \frac{T}{\pi(D - t_l)t_l}, \tag{8}$$

where the weight vector (0, 0, W_z) is $\mathbf{W = W_l\text{-}W_W\text{+}W_f}$ where subscripts, l, w, and f, denote the line's dry weight, buoyancy, and internal fluid's weight; m_e represents the mass of a finite element, which consists of dry mass, fluid's weight, and added mass in the axial direction; $\ddot{r}^t_{k+0.5}$ denotes the tangential acceleration at the element's mid-length, so the calculations of tangential accelerations require displacements at least two time steps; D is the outer diameter; and t_l is the thickness.

Bending stress at the mid-thickness was acquired by using the DNV standard (DNV, 2010)

$$\sigma_M(\theta) = \left[M_{op}(t)\sin(\theta) + M_{ip}(t)\cos(\theta)\right]\left(\frac{D - t_l}{2I}\right) \tag{9}$$

where M_{op} and M_{ip} are out-of-plane and in-plane bending moments; I denotes the second moment of area; and θ is the angle in the circumferential direction relative to the in-plane direction. If $\theta = 0$, the bending stress is solely determined by the in-plane bending moment. DNV (2010) proposed a formulation based on local x and y directions rather than the out-of-plane and in-plane directions. However, many subsequent studies have adopted the out-of-plane and in-plane directional framework, particularly in applications such as chain out-of-plane and in-plane bending. In this study, the out-of-plane direction was defined as the direction normal to both the unit tangent vector and the unit vertical vector, while the in-plane direction was defined as the vector normal to both the unit tangent vector and the out-of-plane direction. Accordingly, the following equations were applied to calculate these bending moments

$$M_{ip,k} = EI\left(\mathbf{r}''_k \cdot \frac{\left(\left(\mathbf{r}'_k \times \mathbf{e_z}\right) \times \mathbf{r}'_k\right)}{\left|\left(\mathbf{r}'_k \times \mathbf{e_z}\right) \times \mathbf{r}'_k\right|}\right) \tag{10}$$

$$M_{op,k} = EI\left(\mathbf{r}''_k \cdot \frac{\left(\mathbf{r}'_k \times \mathbf{e_z}\right)}{\left|\mathbf{r}'_k \times \mathbf{e_z}\right|}\right) \tag{11}$$

where E denotes the modulus of elasticity; and e_z represents the unit vertical vector, i.e., e_z = (0,0,1).

After obtaining the tensile and bending stresses, the nominal stress at the mid-thickness σ_{ZZ} was subsequently calculated as

$$\sigma_{ZZ}(\theta) = \sigma_T + \sigma_M(\theta) \tag{12}$$

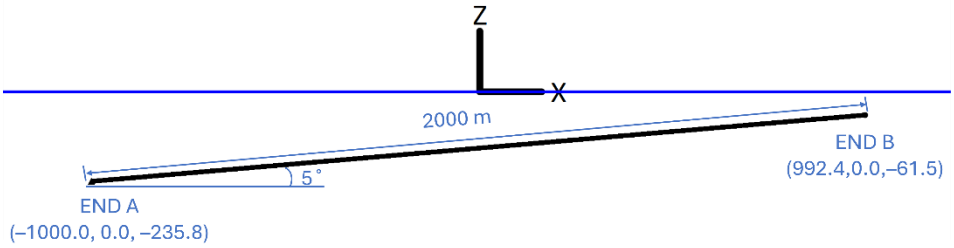

Fig. 4 Configuration of the underwater inclined tunnel (side view) (Jin and Hong 2024)

3. Case study description

This study examined two numerical examples to validate the proposed monitoring method. The first example involved an underwater inclined tunnel, while the second focused on a lazy-wave riser attached to a Floating Production Storage and Offloading (FPSO) vessel, modeled using the commercial program, OrcaFlex. The second scenario posed greater challenges due to the presence of significant initial curvature, inflection points, and slope discontinuities near the touch-down zones, complicating monitoring with discretized sensor arrangements. The OrcaFlex (Orcina 2023), a widely utilized commercial software for analyzing dynamic and structural behaviors of ocean structures, was employed to develop the numerical model and generate both synthetic sensor data and ground truth data for validation of the monitoring method.

3.1 Example 1—underwater inclined tunnel

The first example focused on an underwater inclined tunnel, a structure gaining significant attention in recent years due to the increasing interest in submerged floating tunnels. A side view of the structure is shown in Fig. 4, with its principal design parameters and structural properties detailed in Table 1. For numerical modeling, the lumped mass method connecting line elements by axial, bending, and torsional springs was employed to capture structural elasticity, while the Morison equation was used to account for hydrodynamic loads under wave actions. The long tunnel was discretized into 400 finite elements, each with an equal length of 5 m, to ensure an accurate representation of elastic behavior. The fine division of finite elements was also implemented to generate synthetic sensor data accurately. The detailed methodology underlying the numerical model can be found in the authors' previous study (Jin and Hong 2024).

Two environmental load cases were selected for analysis: Case 1, representing an operating condition, and Case 2, representing a survival condition. The significant wave heights (H_s) for operating and survival conditions were set at 2 m and 11.7 m, with corresponding peak periods (T_p) of 6 s and 13 s. Unidirectional long-crested random waves were generated using the JONSWAP wave spectrum with a fixed enhancement parameter of 2.14. The wave direction was set perpendicular to the tunnel's longitudinal axis to induce maximum displacements. Simulations were conducted for 1-hour durations with a time step of 0.5 s. The water depth is 1500 m and two ends are assumed to be fixed with hinged boundary conditions. Inclined shape, water depth, and boundary conditions in this study could slightly deviate from conventional engineering practices. For instance, horizontally laying submerged floating tunnels with higher buoyancy-to-weight ratios and fixed-fixed boundary conditions have been extensively studied (Kim *et al*. 2023). However, this research

Table 1 Principal design parameters and structural properties of underwater inclined tunnel

Parameter	Value	Unit
Length	2000	m
Outer diameter	10	m
Shell thickness	1.22	m
End boundary condition	Hinged boundary condition	-
Mass/unit length	80.50×10^3	kg/m
Buoyancy to weight ratio	1.0	-
Axial stiffness	1.01×10^{12}	N
Bending stiffness	9.89×10^{12}	Nm^2
Torsional stiffness	8.24×10^{12}	Nm^2
Added mass coefficient	1.0	-
Drag coefficient	0.55	-

prioritizes the verification of the monitoring algorithm by incorporating a design that may induce more complex elastic motions with higher modes, offering a robust evaluation of the algorithm's capabilities.

3.2 Example 2—FPSO with single lazy-wave riser

The second example involved a single lazy-wave riser attached to an FPSO. Fig. 5 illustrates the FPSO and riser configuration in 3D, while Table 2 outlines the principal design parameters and structural properties of the lazy-wave riser. A representative model provided by Orcina, specifically the A01 Lazy Wave Riser with 10" Lazy Wave Distributed example, was utilized. The FPSO and riser in this model were not full-scale representations typical of deep-water operations, as vessel and riser lengths were 103 m and 190 m, respectively. For the FPSO motion calculations, pre-computed six-degree-of-freedom (6-DOF) response amplitude operators (RAOs) were employed. As a result, the riser responses resembled responses under forced vibrations, with no coupled interaction between the FPSO and riser considered. Similar to Example 1, the riser was modeled using the lumped mass method for structural elasticity and the Morison equation for hydrodynamic loads. Again, the lazy-wave riser was discretized into 380 finite elements, each with an equal length of 0.5 m, to ensure an accurate representation of elastic behavior. The lazy-wave riser design incorporated two distinct line properties: one for the pipe alone and another for the pipe equipped with buoyancy modules. Instead of physically adding buoyancy modules to the pipe, adjustments were made to the material properties of the riser such as mass and outer diameter. The riser model included a uniformly distributed internal fluid with a density of 1000 kg/m^3. Additionally, only first-order wave forces were considered in this study, excluding second-order slow-varying wave force and resulting FPSO motions. The environmental conditions and directions were consistent with those in Example 1. The water depth was 100 m and the wave direction in this example was in the positive x direction. Case 3 represents the lazy-wave riser under operating conditions, while Case 4 represents the riser under survival conditions. In this example, the end boundary conditions were different from those of the underwater inclined tunnel. The top point was moving with the vessel motion, and the hinged boundary conditions were applied to both the top and bottom ends.

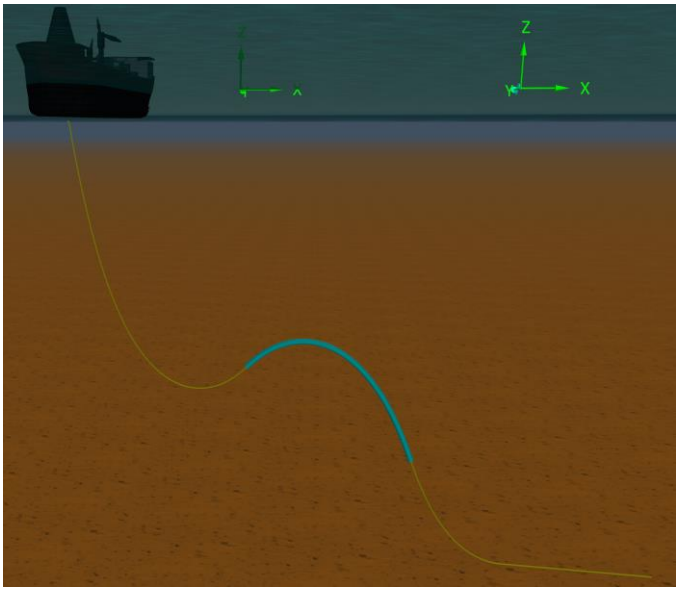

Fig. 5 Configuration of FPSO with single lazy-wave riser

Table 2 Principal design parameters and structural properties of a lazy-wave riser

Parameter	Value		Unit
	Pipe	Pipe with buoyancy module	
Length	First 80 m and last 60 m	Middle 50 m	m
Equivalent outer diameter	0.36	0.81	m
Shell thickness	0.05	0.28	m
End boundary condition	Hinged boundary condition		-
Mass/unit length	184.0	359.3	kg/m
Axial stiffness	7.11×10^8		N
Bending stiffness	1.25×10^5		Nm^2
Added mass coefficient	1.0		-
Drag coefficient	Reynolds-number-dependent drag coefficients		-

4. Results and discussions

The Results and Discussions section compares the ground-truth values obtained from dynamic simulations with the estimated ones from the proposed methodology for both examples. Specifically, it includes the analyses of the envelopes for RMSE, STD, and MAX, along with representative time histories. Key results, such as displacements, nominal stresses, and bending moments, are presented and thoroughly discussed.

Initially, fine intervals of inclinometers were employed to validate the developed monitoring algorithm. With both displacements and curvatures measured at the line's ends, a total of 21 inclinometers were evenly distributed for measurements of angles. In this setup, for the underwater inclined tunnel, the sensor interval was set to 100 m for a tunnel length of 2000 m, while for the lazy-wave riser, the interval was 9.5 m for a riser length of 190 m.

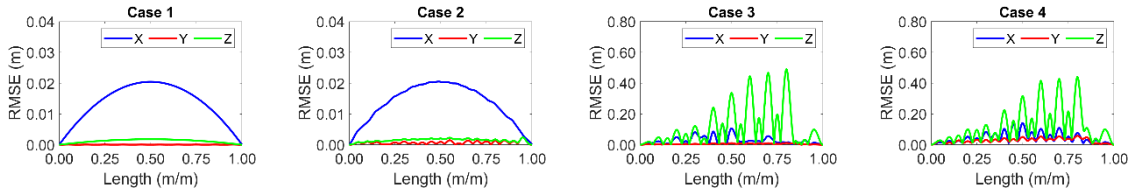

(a) (b) (c) (d)

Fig. 1 Envelopes of RMSEs of *x*, *y*, and *z* displacements for Cases 1–4 (a–d)

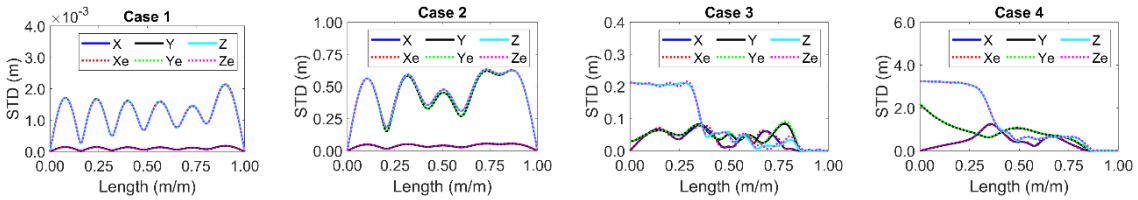

(a) (b) (c) (d)

Fig. 7 Envelopes of STDs of x, y, and z displacements for Cases 1–4 (a–d) (In legend, X, Y, and Z are the reference values from simulations; Xe, Ye, and Ze are estimated values from the monitoring algorithm)

Figs. 6 and 7 present the envelopes of RMSEs and STDs for the *x*, *y*, and *z* displacements across the four cases. In the envelop plots, the *x*-axis is the normalized arc length ($0 \leq$ arc length ≤ 1). It should be recalled that Cases 1 and 2 correspond to the underwater inclined tunnel under significant wave heights of 2 m and 11.7 m, respectively, while Cases 3 and 4 represent the lazy-wave riser cases. For the underwater inclined tunnel, as shown in Figs. 6(a) and 6(b), the *x* displacements exhibit higher RMSE compared to the *y* and *z* displacements. This can be attributed to the tunnel's orientation, as it is predominantly aligned along the longitudinal direction with only a 5-degree inclination. Consequently, even minor errors in the coefficients, *a*, *b*, *c*, and *d* lead to larger errors in the *x* displacement. Notably, these errors are primarily due to the static position rather than dynamic components, as the wave heading is perpendicular to the tunnel's longitudinal direction, and thus the longitudinal displacement is small. In terms of STD comparisons, Figs. 7(a) and 7(b) indicates that *y* and *z* displacements exhibit significantly larger STDs than *x* displacements, reflecting the influence of the wave heading perpendicular to the longitudinal direction. Despite these variations, the estimated displacements align well with the ground-truth values obtained from dynamic simulations.

For the lazy-wave riser, larger RMSE values are observed for the *x* and *z* displacements, as illustrated in Figs. 6(c) and 6(d). The STD comparison in Figs. 7(c) abd 7(d) shows more noticeable differences between the estimated and ground-truth values than the Cases 1 and 2. This difference is more pronounced in the low sea state (Case 3) compared to the high sea state (Case 4), as evidenced by a direct comparison of Figs. 7(a) and 7(b); compared to ground-truth STDs, estimated STDs have higher fluctuations in lower sea state. Despite these minor differences, the general trends and magnitudes align well overall.

To further evaluate the performance of the monitoring algorithms, time histories of the *x*, *y*, and *z* displacements were compared between the ground-truth and estimated values, as shown in Fig. 8. For clarity, only the initial 1000 seconds of results are presented, allowing for a better visualization

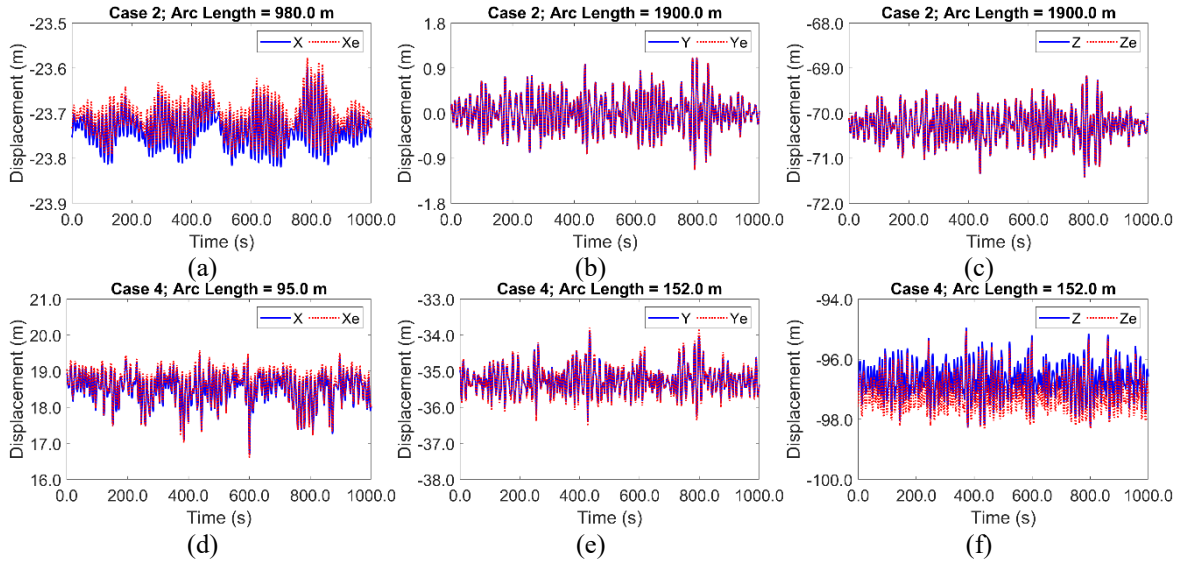

Fig. 2 Time histories of *x*, *y*, and *z* displacements for Cases 2 (a–c) and 4 (d–f) where the largest RMSE is observed. (In legend, X, Y, and Z are the reference values from simulations; Xe, Ye, and Ze are estimated values from the monitoring algorithm)

of the time-history plots. However, the RMSE and STD plots in the paper remain based on the full one-hour simulation. Only cases with larger wave conditions—Cases 2 and 4—are included in this analysis. The representative time histories were extracted at the arc length corresponding to the highest RMSE values (worst case) identified in Fig. 6. From Fig. 8, it is evident that the time histories are accurately reconstructed. The dynamic displacements closely match the ground-truth values, although some discrepancies are observed in the mean position. Specifically, the mean position deviations are approximately 0.02 m for the *x* displacement of the underwater inclined tunnel in Case 2 and 0.1 m and 0.42 m for the *x* and *z* displacements of the lazy-wave riser in Case 4, respectively. These values align with the maximum RMSE values presented in Figs. 6(b) and 6(d). Despite these minor errors, the results confirm the high accuracy of the monitoring algorithms in recovering both dynamic and mean displacements.

Next, nominal stresses were compared, maintaining the same sensor positions and arrangements as those used for the displacement tracing as presented in Figs. 6-8. Nominal stresses were calculated at 30-degree circumferential intervals at every node. For consistency, the nodal positions in the estimation matched those in the ground-truth data, with 421 and 381 nodal positions considered for the underwater inclined tunnel and the lazy-wave riser, respectively.

Fig. 9 presents the envelopes of STDs and MAXs for nominal stresses. At each nodal position, only the maximum nominal stresses along the circumferential arc length among the eight calculated at 30-degree intervals are displayed. A similar trend to displacements is obtained in that the STD and MAX values for the lazy-wave riser exhibit higher fluctuations. The underwater inclined tunnel case achieves higher accuracy due to several factors: it lacks large initial curvature under the neutrally buoyant condition, both ends remain stationary under hinged end boundary conditions, and its mode shape and displacement distribution closely resemble a sinusoidal pattern. In contrast, the lazy-wave riser features sharp curvature near the touchdown point, a large initial curvature due to

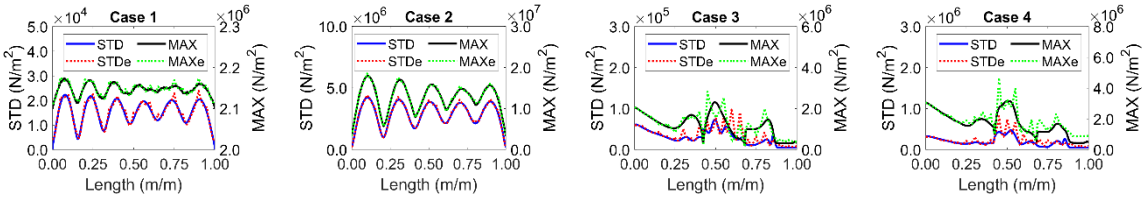

Fig. 9 Envelopes of STDs and MAXs of nominal stresses for Cases 1–4. (In legend, STD and MAX are the reference values from simulations; STDe and MAXe are estimated values from the monitoring algorithm. Left and right y-axes represent STDs and MAXs, respectively)

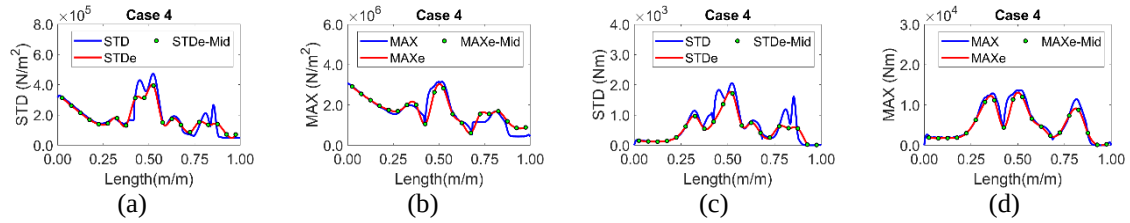

Fig. 10 Envelopes of STDs and MAXs of the stresses (a–b) and bending moment (c–d) for Case 4. (In legend, STD and MAX are the reference values from simulations; STDe and MAXe are estimated values from the spline interpolation using mid-length values; STDe-Mid and MAXe-Mid denote the mid-length values)

the buoyancy module, and one moving end, all of which contribute to reduced monitoring performance. Compared with displacements, the errors of stresses in STD and MAX are much larger, evidently seen in lazy-wave riser cases for which there are sharp variations in curvatures. While displacements are expressed using cubic polynomial equations, the corresponding curvatures vary linearly for each segment; it introduces larger errors in stress distributions than displacement ones, especially in regions with sharp curvature variations. When sensor intervals are large, this linear assumption cannot adequately capture curvature variations, particularly in regions where the curvature changes significantly along the arc length.

Due to the nontrivial errors in stress estimations with significant variations in initial curvature, an alternative remedy was devised with a focus on the accuracy improvement of bending stresses. In the Hermite cubic spline function, widely used for beam finite element interpolation, curvatures at the mid-arc length are estimated using only the angles at both ends. Since inclinometers were employed in this study, relatively stable curvatures at the mid-lengths of finite elements could be directly obtained, albeit with potential errors due to sensor intervals. In this regard, as a remedy for stress estimation, curvatures at the mid-lengths were first extracted from the monitoring algorithm at each time step, and between these two curvature points, cubic spline interpolation was applied.
As shown in Fig. 10, the proposed remedy partially achieves its intended goal. While discrepancies remain in regions with sharp curvature changes, the high fluctuations observed in Fig. 9 are no longer present. These errors could be further mitigated by adopting variable sensor intervals, i.e., more sensors near sharper variations of curvatures. Additionally, the comparison clearly demonstrates that stress at initial arc lengths is primarily induced by tension while bending stresses dominate at larger arc lengths. From the stress and bending moment comparisons, the accuracy of the proposed method for indirect tension estimation is also indirectly validated.

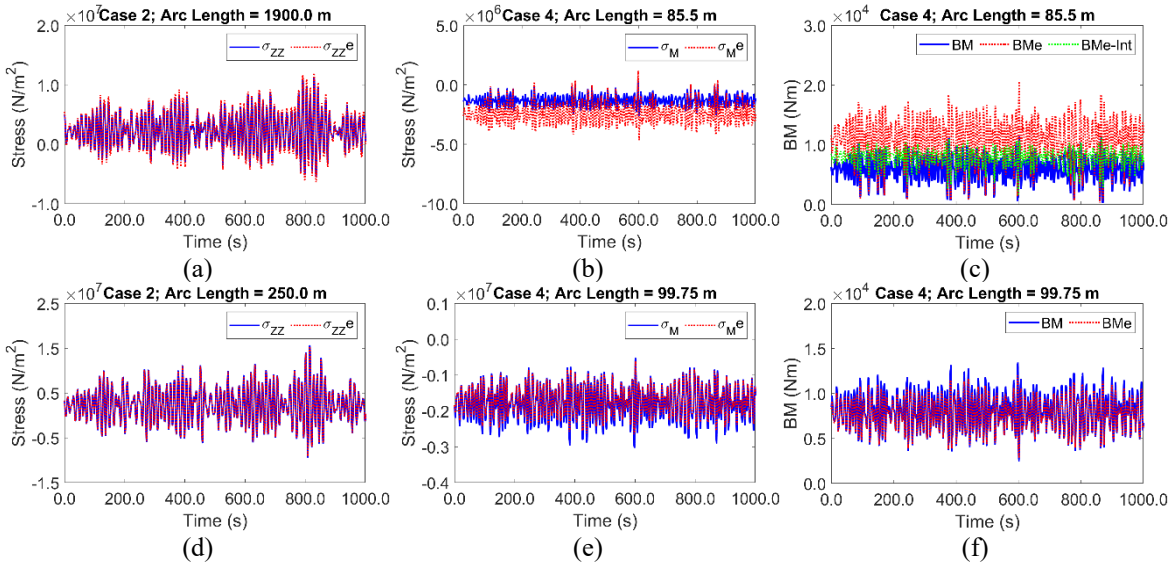

Fig. 3 Time histories of nominal stresses for Cases 2 (a and d) and 4 (b and e) and bending moment for Case 4 (c and f). (a) and (b) are the time histories where the largest RMSE is observed among all nodal positions; (c) corresponds to (b); (b) and (d) are the time histories where the largest STD is observed among all mid-length positions between neighboring inclinometers; (f) corresponds to (e). (In legend, σ_{ZZ} and BM are the reference values from simulations; σ_{ZZ}e and BMe are the estimated values from the monitoring algorithm; BMe-Int denotes the interpolated value from neighboring mid-length values)

Fig. 11 presents the representative time histories of nominal stresses for Cases 2 and 4 as well as the bending moments for Case 4. The stresses at the position with the highest RMSE along the entire arc length are shown in Figs. 11(a) and 11(b). Consistent with the trends observed in Fig. 9, Case 2 shows a minor discrepancy between the ground-truth and estimated stresses, while Case 4 reveals a more significant deviation. However, when examining the stresses at the arc length with the highest STD among all the mid-length positions between neighboring inclinometers, both cases display similar trends and magnitudes, as illustrated in Figs. 11(d) and 11(e). Moreover, while the bending moment comparison shown in Figs. 11(c) and 11(f) leads to similar conclusions as the stress analysis, the cubic interpolation of bending moments from mid-length values can enhance the accuracy of the estimation, as clearly seen in Fig. 11(c). This finding underscores the effectiveness of the monitoring algorithm in accurately capturing the dynamic behavior of nominal stresses at mid-length positions, even with variations in RMSE and STD patterns along the arc length.

Finally, the sensitivity of the proposed methodology to sensor intervals was examined, as illustrated in Fig. 12. The baseline results for the underwater inclined tunnel and lazy-wave riser were based on sensor intervals of 100 m and 9.5 m, respectively. For this analysis, both shorter and longer sensor interval cases were considered, and the RMSE was compared. The RMSE presented in this figure represents the mean RMSE across all nodal positions, while the RMSE for mid-length stresses corresponds to the mean RMSE across all mid-length positions between adjacent inclinometers. Only Cases 2 and 4 are included in this comparison. Overall, smaller sensor intervals generally resulted in higher accuracy, as indicated by lower RMSE values. In stress comparisons, mid-length stresses demonstrated better estimation accuracy, similar to Fig. 10.

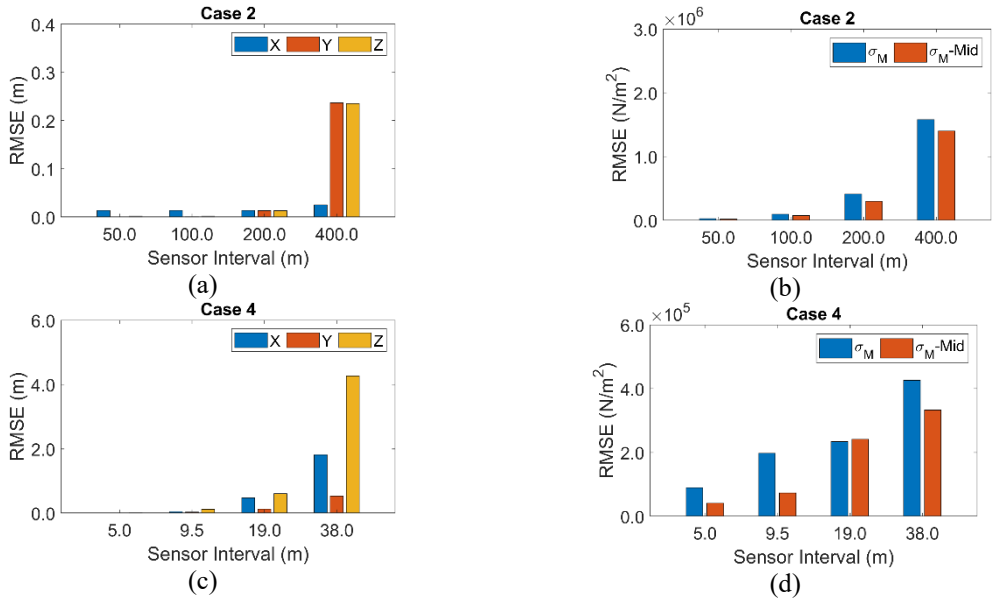

Fig. 4 RMSEs of x, y, and z displacements (a and c) as well as nominal stresses (b and d) for Case 2 (a–b) and 4 (c–d) with respect to sensor intervals. RMSEs are the mean RMSEs across all nodal positions. Mid in the legend denotes the mean RMSE across all the mid-lengths between neighboring inclinometers

While the present study primarily focuses on verifying the proposed methodology, several potential improvements and sensitivity analyses are suggested for future work. First, a compromise in sensor intervals can be explored. For instance, results appear consistent for intervals up to 200 m and 19 m for Cases 2 and 4, respectively, whereas intervals of 400 m and 38 m significantly increase the RMSE. Through this analysis, appropriate sensor intervals with good accuracy and a small number of sensors can be found. Additionally, identifying the optimal sensor interval can further enhance performance. Optimally placed inclinometers may achieve comparable results with fewer sensors compared to uniformly distributed sensor cases, as demonstrated by Jin and Hong (2024). Moreover, with the same number of sensors, the current use of cubic polynomial equations can be extended to fourth-order polynomial equations. This approach would involve merging two finite elements into one and formulating the additional equation using the unit tangent vector at the mid-length, enabling a curvature to be expressed as a quadratic polynomial equation. Furthermore, the algorithm can calculate accumulated fatigue damage from time-domain fatigue assessment. These promising directions will be explored in future studies.

5. Conclusions

This study proposes a monitoring methodology using cubic polynomial equations and sensor fusion to evaluate the global behavior and stress distribution of underwater lines. The approach integrates generalized coordinates into a single global coordinate system, enabling efficient capture of the behavior of geometrically complex lines. The system requires input data, including displacements and curvatures at both ends, as well as inclinations along the line, which serve as

boundary conditions for the cubic polynomial equations for displacements. Using the computed global displacements, tensile, bending, and nominal stresses are subsequently estimated. The following key conclusions are drawn:

- The proposed methodology was validated through numerical case studies of two underwater lines: the submerged inclined tunnel and the lazy-wave riser. Both cases demonstrate that the methodology can effectively capture global displacements and stress distributions.
- Results from the underwater inclined tunnel show higher accuracy in displacement and stress estimation compared to the lazy-wave riser, which exhibits larger errors due to its initial sharp curvature near the lazy-wave zone and touchdown point.
- In case of sharp variation of curvature along arclength, like the lazy-wave riser case, the use of analytic mid-length bending stress can improve the stress estimation.
- Monitoring performance for both cases was affected by sensor intervals, with finer sensor spacing leading to more accurate results.

Further improvements are needed for the developed methodology, particularly in addressing the challenges posed by highly curved structures like the lazy-wave risers. Therefore, future research will focus on optimizing sensor intervals and exploring the extension of the order of polynomial equations. Additionally, studies will focus on optimal sensor placement strategies to reduce the number of sensors while maintaining accuracy. Furthermore, the feasibility of increasing the order of the polynomial equation will be explored to better estimate stresses. Finally, fatigue damage calculations will be conducted to assess the error in fatigue life estimation at critical hot spots.

Acknowledgments

Research reported in this publication was supported by an Early-Career Research Fellowship from the Gulf Research Program of the National Academies of Sciences, Engineering, and Medicine. The content is solely the responsibility of the authors and does not necessarily represent the official views of the Gulf Research Program of the National Academies of Sciences, Engineering, and Medicine.

References

Bakker, M., (2011), "An alternative methodology for riser lifetime prediction", Master's Thesis, Department of Offshore Engineering, Delft University of Technology, Delft, The Netherlands.

Chen, K., Yang, J., Yin, Q., Mayank, T., Gao, B., Song, Z., Jia, S., Liu, S., Xie, B. and Chen, H., (2024), "Digital twin: Hybrid virtual simulation and physical monitoring strategy for long-term safe operation of floating production platform-hybrid polyester mooring lines-steel catenary risers multibody System in the South China sea", *Proceedings of the Offshore Technology Conference*, Houston, USA, OTC, D041S052R007.

Choi, J. and Kim, J.M.H. (2018), "Development of a new methodology for riser deformed shape prediction/monitoring", *Proceedings of the International Conference on Offshore Mechanics and Arctic Engineering*, American Society of Mechanical Engineers, V005T004A041.

Chung, W.C., Jin, C. and Kim, M. (2022), "Dual-algorithm hybrid method for riser structural health monitoring using the fewest sensors", *J. Mar. Sci. Eng.*, **10**(12), 1994. https://doi.org/10.3390/jmse10121994.

Chung, W.C., Kim, M. and Jin, C. (2021), "Real-time trace of riser profile and stress with numerical inclinometers", *Ocean Eng*., **234**, 109292. https://doi.org/10.1016/j.oceaneng.2021.109292.
DNV, (2010), "Recommended practice DNV-RP-F204-Riser fatigue", *Hovik, Norway*.
Garrett, D.L. (1982), "Dynamic analysis of slender rods", *J. Energ. Resour. Technol.*, **104**(4), 302-306. https://doi.org/10.1115/1.3230419.
Jin, C. and Hong, S.H. (2024), "Underwater line monitoring using optimally placed inclinometers", *J. Mar. Sci. Eng*., **12** (11), 1939.
Jin, C., Kim, S.J., Kim, M., Lee, Y., Guha, A., Ryu, S. and Xu, W. (2024), "Real-time dynamic and structural behavior estimation of a steel lazy wave riser through finite-element-based digital twin and hull-motion sensor", *Appl. Ocean Res*., **150**, 104137. https://doi.org/10.1016/j.apor.2024.104137.
Jin, Y., Wei, M., Mengbiao, Y., Deli, G., Bo, Z. and Yunjin, X. (2015), "Calculation method of riser top tension in deep water drilling", *Petrol. Explor. Development*, **42**(1), 119-122. https://doi.org/10.1016/S1876-3804(15)60014-3.
Kaasen, K.E. and Lie, H. (2003), "Analysis of vortex induced vibrations of marine risers", *Model. Ident. Control*, **24**, 71-85. https://doi.org/10.4173/mic.2003.2.1.
Kharazmi, E., Wang, Z., Fan, D., Rudy, S., Sapsis, T., Triantafyllou, M.S. and Karniadakis, G.E. (2021), "From data to assessment models, demonstrated through a digital twin of marine risers", *Proceedings of the Offshore Technology Conference*, OTC, D031S035R003.
Kim, H., Jin, C. and Kim, M. (2021), "Real-time estimation of riser's deformed shape using inclinometers and Extended Kalman Filter", *Mar. Struct.*, **77**, 102933. https://doi.org/10.1016/j.marstruc.2021.102933.
Kim, S.J., Jin, C., Lee, I., Kim, G.J., Kim, M. and Kwak, H.G. (2023), "Efficient time-domain approach for hydroelastic-structural analysis including hydrodynamic pressure distribution on a moored SFT", *Mar. Struct.*, **90**, 103402. https://doi.org/10.1016/j.marstruc.2023.103402.
Lee, Y., Jin, C., Kim, M. and Xu, W. (2024), "Digital twin approach with minimal sensors for riser's fatigue-damage estimation", *Int. J. Naval Architect. Ocean Eng.*, **16**, 100603. https://doi.org/10.1016/j.ijnaoe.2024.100603.
Mao, Y., Wang, T. and Duan, M. (2022), "A DNN-based approach to predict dynamic mooring tensions for semi-submersible platform under a mooring line failure condition", *Ocean Eng*., **266**, 112767. https://doi.org/10.1016/j.oceaneng.2022.112767.
McNeill, S. and Agarwal, P. (2011), "Efficient modal decomposition and reconstruction of riser response due to VIV", *Proceedings of the International Conference on Offshore Mechanics and Arctic Engineering*.
Mercan, B., Campbell, M. and Thompson, C. (2021), "Fatigue monitoring and life extension for top tensioned production riser systems", *Proceedings of the Offshore Technology Conference*, OTC, D021S017R006.
Min, S., Jeong, K., Lee, Y. and Kim, S. (2023), "Estimation of unmeasured structural responses of submerged floating tunnels using pattern model trained via long short-term memory", *Ocean Eng.*, **277**, 114284.
Mukundan, H., Hover, F. and Triantafyllou, M. (2010), "A systematic approach to riser VIV response reconstruction", *J. Fluids Struct*., **26**(5), 722-746. https://doi.org/10.1016/j.jfluidstructs.2010.04.001.
Orcina, L. (2023), OrcaFlex User Manual Version 11.4.
Saruhashi, T., Kluk, D.J., Kyo, M., Bhalla, K., Sawada, I., Miyazaki, E., McNeill, S. and Yamazaki, Y. (2013), "Development of a real-time riser fatigue monitoring system", *Proceedings of the Offshore Technology Conference*, OTC, OTC-24216-MS.
Wang, J., Sheng, L., Geng, Y., Wang, M., Wang, Y., Li, Y. and Liu, X. (2023), "Fatigue damage assessment methodology for a deepwater subsea wellhead based on monitoring data", *Ships Offshore Struct.*, **19**(10), 1-13. https://doi.org/10.1080/17445302.2023.2260956.